Theta Phase Precession Emerges from a Hybrid Computational Model of a CA3 Place Cell:

Supplementary Description of the Computational Model

John L Baker
Neuroscience Doctoral Program,
George Mason University, Fairfax VA, 22030 USA

James L Olds
The Krasnow Institute for Advanced Study,
George Mason University, Fairfax VA, 22030 USA

Corresponding author:

John L Baker (jbakerb@gmu.edu)

The Krasnow Institute for Advanced Study
George Mason University
4400 University Drive, MS 2A1
Fairfax, Virginia 22030 USA

Overview

These supplementary materials provide a description for the computational model used in the associated research article. Source code for the model is publicly available via ModelDB (Hines et al., 2004) and contains additional commentary on the structure and rationale of the model.

The model described here simulates movements of a mouse in a maze and from this generates representative spike trains afferent to a single "target" CA3b pyramidal cell. Mouse movement and afferent spike trains are generated using phenomenological models while the target pyramidal cell is simulated using a biophysically realistic compartmental model (Figure S1).
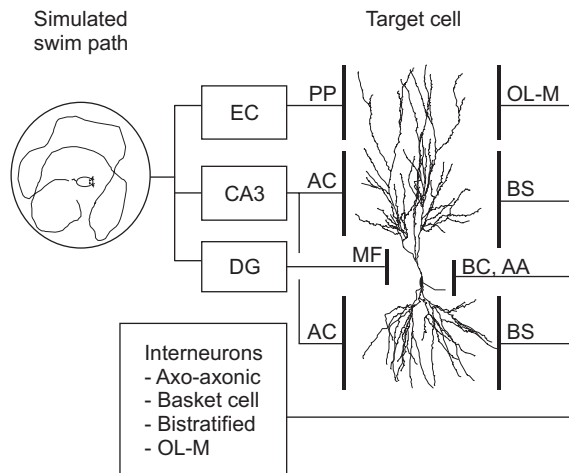

Figure S1. General model schematic showing afferent cell groups and target cell relationship. Place cell firing is determined by the location of a simulated animal moving within a maze. Afferent cell groups are entorhinal cortex (EC), which provides perforant path (PP) inputs, CA3 peer pyramidal cells, which provide associational connection (AC) inputs, and dentate gyrus (DG) granule cells, which provide mossy fiber (MF) inputs. Interneurons are divided into four separate population subgroups: axo-axonic cells (AA), basket cells (BC), bistratified cells (BS), and cells with soma in the stratum oriens and axons in strata lacunosum-moleculare (OL-M). This is figure also appears in the main body of the article and is included here for completeness.

A primary objective of the combined model is to allow realistic modeling of CA3 pyramidal cell responses to *in vivo* conditions without incurring the cost and complexity of simulating the entire hippocampus or other associated brain regions.

Simulated Environment

The simulated environment used in the current model has been chosen to be similar to an experiment that demonstrates the critical nature of synaptic plasticity in CA3 (Nakazawa et al., 2002). A simulated mouse moves within a 50-cm square maze in which movement is restricted to a counter-clockwise path that maintains a roughly constant distance from the maze boundary. Throughout the simulation, the mouse moves at a constant speed of 10 cm/sec.

Afferent Place Cell Firing Models

A phenomenological model of afferent place cell firing is used to provide inputs to the target cell. As the simulated mouse moves through the maze, the simulated firing rates of cells in entorhinal cortex (EC), dentate gyrus (DG), and CA3 pyramidal cells vary based on the current location and heading of the mouse. Instantaneous firing rates are used to generate each afferent cell's spike train as an inhomogenous Poisson process with a minimum refractory interval of 5 ms through the use of a spike thinning algorithm (Dayan and Abbott, 1971).

Location specific firing rates are determined using a phenomenological model of place field firing similar to prior hippocampal models (O'Keefe and Burgess, 1996; Wallenstein and Hasselmo, 1997; Hartley et al., 2000; Káli and Dayan, 2000). The place cell model used here is generalized to support arbitrary maze geometry. For each afferent place cell, a

local spatial coordinate system is imposed with its origin at the place field center and one axis oriented towards the maze boundary point nearest the cell's place field center. Afferent place cell firing rates are formulated in terms of the corresponding local coordinate system using the relationship

$$\sigma_X = \sigma_0 + \rho_{dist}|b_X|,$$
$$\sigma_Y = \sigma_0 + \rho_{dist}|b_Y|, \quad (1)$$
$$F_{loc}(x,y) = \frac{F_{avg}}{2\pi\sigma_X\sigma_Y}\exp\left[\frac{-x^2}{2\sigma_X^2} + \frac{-y^2}{2\sigma_Y^2}\right]$$

where b_X and b_Y are the distance to the closest maze boundary along the local coordinate X and Y axes, σ_X and σ_Y are derived standard deviates, σ_0 is the minimum standard deviate, σ_{dist} reflects the relative error in distance estimates, F_{loc} is the location-dependent firing rate at local coordinates (x,y), and F_{avg} is the theoretical mean firing rate for the place cell. Parameters σ_0, ρ, and F_{avg} are parameters of the population (EC, DG, or CA3) of which the place cell is a member while b_X and b_Y are specific to the individual place cell. Place field center locations for afferent place cells are chosen randomly with a uniform distribution throughout the interior of the maze.

Place cell firing is affected by rhythmic theta and gamma oscillatory patterns (Buzsáki, 2002; Csicsvari et al., 2003) and the phenomenon of theta phase precession (O'Keefe and Recce, 1993). Let (x,y) be the current position of the simulated animal, let (h_x,h_y) be a unit vector indicating the current heading, and let t be the current time. The instantaneous firing rate of a given place cell is then found by

$$\Delta_\theta = \theta_{PC} + \rho_{tpp}(x \cdot h_x + y \cdot h_y),$$
$$F(t,x,y) = F_{loc}(x,y)$$
$$\times[1 + A_\theta\cos(2\pi f_\theta \cdot t - \Delta_\theta)] \quad (2)$$
$$\times[1 + A_\gamma\cos(2\pi f_\gamma \cdot t)]$$

where θ_{PC} is the peak firing theta phase for the cell type, Δ_θ is the combined theta phase offset including theta phase precession, ρ_{tpp} is the linear rate of phase precession, A_θ is the amplitude of theta modulation, $f_\theta = 8$ Hz is the frequency of theta oscillation, , $A\gamma$ is the amplitude of gamma modulation, $f\gamma = 40$ Hz is the frequency of gamma oscillation, $F_{loc}(x,y)$ is the location-dependent firing rate, and $F(t,x,y)$ is the derived instantaneous firing rate at time t and location (x,y) for the given afferent place cell.

Place cells properties are chosen to generally reflect experimental findings. The associated place field has been adjusted because of the smaller mazes used here. Dentate gyrus place cells are spatially selective and have low average activity rates (Jung and McNaughton, 1993; Skaggs et al., 1996). CA3 place cells are intermediate in spatial selectivity and activity (Muller, Kubie, and Ranck, 1987; Brazhnik, Muller, and Fox, 2003; Vazdarjanova and Guzowski, 2004). Entorhinal cortex place cells are modeled with properties similar to those of CA3 place cells (Fyhn et al. 2004; see also Quirk et al, 1992). Peak theta phase firing for each type of place cell is similarly chosen based upon experimental findings (Fox, Wolfson, and Ranck, 1986; Stewart, Quirk, Barry, and Fox, 1992). Tables S1 and S2 summarize parameters used in modeling afferent place cells.

Interneuron Firing Models
Because interneuron firing is minimally affected by location and heading, F_{loc} is constant and the theta phase precession rate K_{TPP} is zero for interneurons, allowing formula (2) to be applied without change.

Table S1. Afferent cell group network parameters

Afferent Cell Group	Group Pop Size	Active Freq (Hz)	Peak Theta Phase	Theta Mod (A_θ)	Gamma Mod (A_γ)	Target Cell Synapses (typical)	Synapse Laminar Extent (μm)	Synapse Receptor Types
EC II-III	2,000	2	5°	1.0	0.5	1,348	350-500 apical	AMPA, NMDA
DG	4,000	1	296°	1.0	0.5	43	0-100 apical	AMPA, NMDA
CA3 Peer	12,000	2	19°	0.75	0.2	5,362	100-350 apical	AMPA, NMDA
						4,622	0-300 basal	AMPA, NMDA
Axo-axonic	100	17	185°	1.0	0.0	200	IS	$GABA_A$
Basket Cell	100	8	271°	0.6	0.0	200	soma	$GABA_A$
Bistratified	500	6	359°	1.0	0.0	2,565	all dendrites	$GABA_A$, $GABA_B$
OL-M	100	5	19°	0.8	0.0	335	350-500 apical	$GABA_{AS}$, $GABA_B$

Laminar extent is measured from the target cell soma in apical or basal directions. Active frequency is approximate, depending on maze and path. The number of target cells synapses varies based on random assignments. Abbreviations: population (pop), frequency (freq), modulation (mod), initial segment (IS), $GABA_A$ slow ($GABA_{AS}$). This is table also appears in the main body of the article and is included here for completeness.

Table S2. Afferent place field spatial parameters

Afferent Cell Group	Fraction Active	F_{avg} (Hz)	σ_0 (cm)	ρ_{dist}	ρ_{tpp} (deg/cm)
EC II-III	100%	0.4	3.5	0.15	10
DG	5%	0.2	2.0	0.10	10
CA3 Peer	18%	0.4	3.5	0.15	10

Abbreviations and symbols: average firing rate when no boundaries are present (F_{avg}), minimum standard deviate for firing rate Gaussian function (σ_0), standard deviate distance ratio (ρ_{dist}), theta phase precession spatial rate (ρ_{tpp}), degrees (deg).

Peak theta phase and nominal firing rate are derived from experiments by Klausberger et al. (2003, 2004) and are shown in Table S1. While basket cell population rates are approximately sinusoidal, as assumed in formula (2), a better approximation of population activity at theta frequencies is a saw-tooth wave. In the current model, basket cell theta frequency modulation is based on such a saw-tooth variation consisting of straight-line rising and falling intervals that has a minimum average firing rate near 0° theta phase and a maximum at 271°, as indicated in Table S1.

Interneuron firing rates are assumed to be variable in response to afferent stimulation, brain state, and environmental novelty (Wilson and McNaughton, 1993; Klausberger et al., 2003, 2004). Interneuron afferents are not explicitly included in the current model, but interneuron firing rates are modulated by a long-term average of the target cell firing rate. Target cell firing rates are estimated using a kernel smoothing function with a decay time constant of 60 sec. Interneuron firing rates of basket cell and bistratified interneurons are specified by the relationship

$$F_{IN} = F_{base} + \frac{F_{inc}}{1 + \exp\left(-\dfrac{F_{TC} - F_h}{k_{IN}}\right)} \quad (3)$$

where F_{IN} is the instantaneous interneuron firing rate, F_{base} is the baseline interneuron firing rate appearing in Table S1, F_{inc} is the maximum firing rate increment, F_{TC} is the smoothed target cell firing rate, $F_h = 3$ Hz is a half-increment rate parameter, and $k_{IN} = 0.5$ Hz is a firing rate sensitivity parameter. F_{inc} is estimated based on the difference in firing rates between theta and sharp-wave ripple states (Klausberger et al, 2003, 2004). F_{inc} has a value three times the baseline rate for basket cells and bistratified interneurons and is zero otherwise.

4

It should be noted that individual interneurons have diverse firing patterns based on their individual characteristics and afferent stimulation (Fox, Wolfson, Ranck Jr., 1986; Klausberger et al, 2003, 2004). The present model is limited to reproducing interneuron population activity on the assumption that proximate excitatory and inhibitory synapses show minimal high-order temporal correlations as they impinge upon the target pyramidal cell.

Target Cell Compartmental Model
Morphology of the target cell (Figure S1) is derived from the morphology of cell L56a as described in the Duke/Southampton Cell Archive (Turner et al., 1995). The cell morphology file for cell L56a in SWC format was converted for use in a compartmental model (Segev and Burke, 1998) in which cylindrical compartments representing dendritic segments have a length of approximately 50 μm and a radius that conserves the membrane area implied by measurements of the corresponding portion of the dendrite from the morphology file. Compartments are constrained such that dendrite branches only appear as connections between compartments. Along a compartment, the corresponding largest and smallest radius values from the SWC file differ by no more than 25%. During the conversion process, compartments are subdivided as needed to meet these constraints. The target cell soma is modeled as a spherical compartment with a membrane area of 1645 μm^2.

Only the soma and dendrites are converted from the SWC morphology file. An initial segment (IS) and axon segment have been added to the target cell model to allow the simulation of both axonal contributions to cell firing and inhibitory effects on the initial segment. The initial segment model consists of a single compartment with length 30 μm and radius

0.7 μm. Ten axon compartments are connected one to another, each with a length 30 μm and a radius that tapers from 0.5 μm in the most proximal axonal compartment down to 0.2 μm in the most distal axonal compartment simulated.

Passive parameters of the target cell have been chosen so that passive membrane properties in combination with ion channels yield properties near rest similar to passive whole cell properties of CA3 pyramidal cells at physiological temperatures (Spruston and Johnston, 1992). When acetylcholine (ACh) is present as a modulator, a non-selective mixed-cation channel is assumed to be opened such that the target cell is depolarized but otherwise experiences minimal change in passive properties (Guérineau, Bossu, Gähwiler, and Gerber 1995). Passive properties of the axon have been chosen based on minimal active repolarization of the axon (Colbert and Pan, 2002) and axon response to somatic stimulation. Table S3 summarizes the passive cell parameters used in the target cell model.

Intracellular calcium dynamics are modeled using the scheme described by Jaffe et al. (1994) with adjustments for more recent results regarding dendritic calcium dynamics (Sabatini, Oertner, Svoboda, 2002). Table S4 contains parameters used in modeling target cell calcium dynamics.

Calcium microdomains near the cell membrane are modeled as a single thin

Table S3. Target cell passive parameters

Parameter	Value
Membrane capacitivity	1 $\mu F/cm^2$
Membrane resistivity	200 Kohm-cm^2
Membrane resistivity (axon)	750 ohm-cm^2
Axial resistivity	100 ohm-cm
Leakage reversal potential	-90 mV
Leakage reversal for axon	-74 mV
Mixed-cation conductivity	0.0015 mS/cm^2
Mixed-cation reversal	0 mV

Table S4. Calcium pool model parameters

Parameter	Value
Internal calcium rest	50 nM
External calcium	2 mM
Unbound ion ratio	0.013 (κ_B=75)
Pump half-activity value	2 µM
Maximum pump rate	$1.5 \cdot 10^{-12}$ mM·ms^{-1}·cm^{-2}
Microdomain subshell depth	0.1 µm

subshell in which calcium is assumed to be of well mixed. Only high- and medium-voltage activated calcium channels influxes contribute to the microdomain subpool concentration since these are the channels coupled with calcium-activated potassium channels (Marrion and Tavalin, 1998). While experimentally relevant, overall calcium concentration outside the microdomain does not play an active role in the current model. Calcium flux through channels is assumed to follow the Goldman-Hodgkin-Katz (GHK) formula as rewritten by Jaffe et al. to allow incorporation of experimentally measured calcium channel conductance

$$I_{CA}(V) = g_{Ca} V \frac{1 - \dfrac{[\text{Ca}^{2+}]_{in}}{[\text{Ca}^{2+}]_{out}} \exp\left(\dfrac{zFV}{RT}\right)}{1 - \exp\left(\dfrac{zFV}{RT}\right)} \quad (4)$$

where I_{Ca} is the calcium current, g_{Ca} is the effective conductance of the calcium channel, V is the membrane potential, $[\text{Ca}^{2+}]_{in}$ is the intracellular calcium ion concentration, $[\text{Ca}^{2+}]_{out}$ is the extracellular calcium concentration, z is the ion charge (+2 for calcium), F is Faraday's constant, R is the gas constant, and T is the absolute temperature. It should be noted that the GHK formula is based on assumptions that are not entirely satisfied by calcium channel pores. The accuracy of the formula as a predictor of currents in some calcium

channels may be limited (Brown et al., 1993).

Ion channels are modeled using the Hodgkin-Huxley independent gating model (Hodgkin and Huxley, 1952). Individual channel gates are modeled using a variation on the extended form of Hodgkin-Huxley equations proposed by Borg-Graham (1999). For a gating state variable X, dynamics are determined through the system of equations

$$\alpha_{bolt} = r \exp\left[\gamma \cdot (V - V_{half})/k\right],$$
$$\beta_{bolt} = r \exp\left[-(1-\gamma) \cdot (V - V_{half})/k\right],$$
$$X_\infty(V) = \frac{\alpha_{bolt}}{\alpha_{bolt} + \beta_{bolt}},$$
$$\tau(V) = \frac{Q_{10}^{(T_{rated}-T)/10}}{\alpha_{bolt} + \beta_{bolt}} + \tau_0, \quad (5)$$
$$\alpha_X = \frac{X_\infty(V)}{\tau(V)}, \quad \beta_X = \frac{1 - X_\infty(V)}{\tau(V)},$$
$$\frac{dX}{dt} = \alpha_X \cdot (1 - X) + \beta_X \cdot X$$

where k is the voltage sensitivity measured experimentally, α_{bolt} and β_{bolt} are theoretical activation and deactivation rates, α_X and β_X are corresponding rates for X adjusted to allow for a rate limiting process and the simulation temperature, τ_0 is a rate limiting time constant, r a gating rate parameter, V is the membrane potential, V_{half} is the half-activation voltage, γ is the relative energy barrier location, T_{rated} is the absolute temperature at which gating kinetics were measured, T is the simulated temperature, Q_{10} is a temperature correction parameter, and $\tau(V)$ and $X_\infty(V)$ are the voltage-dependent time constant and equilibrium values of X. The rate value r is more conveniently expressed in terms of the time constant τ_{max}, which is the maximum value of $\tau(V)$ for any voltage. Simulation software automatically derives the value for r from τ_{max} and other gating parameters.

ACh modulation is modeled based on the effect of muscarinic receptor activation on the peak channel conductance of modulated channels using a method adapted from an earlier model of ACh effects (Menschik and Finkel, 2000) with the following formula

$$g_{mod} = g_{max}\left(1 + A\frac{[ACh]}{[ACh]+Kd}\right) \qquad (6)$$

where g_{mod} is the peak channel conductance after modulation is applied, g_{max} is the specified peak conductance before modulation, [ACh] is the extracellular ACh concentration, A the maximum effect for this channel, and Kd the concentration at which the effect is half the maximum.

Table S5 contains parameters for ion channels using the extended Hodgkin-Huxley formulation above. Ion channel currents are derived using Ohm's law except for calcium channels, in which case the GHK formula is applied. The simulation software applies adjustments to channel kinetic properties using an assumed brain temperature of 37 °C.

The target cell model utilizes multiple models of transient sodium channels (NaT) to represent regional variations in channel properties. Transient sodium channels in dendrites (Magee and Johnston, 1995; Pan and Colbert, 2001; Gasparini and Magee, 2002) are modeled separately from those in the soma and the axon (Colbert and Pan, 2002). For non-axonal sodium channels, slow inactivation is included in the model (Mickus, Jung, and Spruston, 1999). Persistent sodium currents (NaP) are also included in the model and are modeled as a simplified representation of results from channels found in the entorhinal cortex cells (Magistretti and Alonso, 1999, 2002).

Fast inactivation of transient sodium channels is not well fit by equation (4) because of the interaction between channel opening and inactivation (Gasparini and Magee, 2002). The expression for h-gate deactivation is amended to be

$$\beta_h(t) = \beta_h(V) + k_{act}m^3(t) \qquad (7)$$

where k_{act} = 1.5/ms is the contribution of channel open states to inactivation. Transient sodium channel slow inactivation is incomplete and the slow inactivation s-gate variable is rescaled by amending the steady-state voltage sensitivity of slow inactivation to be

$$s_\infty(V) = 0.12 + 0.78\frac{\alpha_{bolt}}{\alpha_{bolt}+\beta_{bolt}} \qquad (8)$$

where the value 0.12 is chosen so that the product of steady-state h and s gating values is approximately a Boltzmann function of voltage conforming with experimental measurements of sodium channel inactivation. When the ACh is present, slow inactivation is inhibited in somatic and proximal dendritic sodium channels but not distal dendritic sodium channels (Tsubokawa and Ross, 1997). When ACh is present at concentrations exceeding 0.1 μM, s_∞=0.6 for somatic and proximal dendritic sodium channels.

The model of Ih currents is derived from the characterization by Magee (1998). Extracellular concentrations of sodium affect properties of this channel including a shift in voltage sensitivity, altered time constants, and reversal potential. To the extent possible, the current model of Ih is derived from experimental results using near physiological solutions.

Delayed rectifier (Kdr) and transient forms (K-A) of potassium channels included in the target cell model have the voltage sensitivity measured by Hoffman, Magee, Colbert, and Johnston (1997). Peak conductance of these potassium channel

Table S5. Target cell ion channel model parameters

Channel Type	g_{max} (mS/ cm^2)	V_{rev} (mV)	ACh A	ACh Kd (μM)	Gating Terms	Gate Var	γ	V_{half} (mV)	k (mV)	τ_{max} (ms)	τ_0 (ms)	Temp (°C) / Q_{10}
NaT soma and IS	30.0	+55.0	-0.35	95	m^3hs	m	0.5	-42.9	8.4	0.2	0.05	22 / 4.0
						h	0.2	-50.0	-8.0	45	0.4	22 / 2.0
						s	0.5	-66.0	-5.3	1300	800	37 / 2.0
NaT prox	40.0	+55.8	-0.35	95	m^3hs	m	0.5	-25.5	10.0	0.2	0.05	22 / 4.0
						h	0.2	-50.0	-8.0	45	0.4	22 / 2.0
						s	0.5	-66.8	-6.8	1300	800	37 / 2.0
NaT distal	10.0	+54.4	-0.35	95	m^3hs	m	0.5	-34.1	10.1	0.2	0.05	22 / 4.0
						h	0.2	-50.0	-8.0	45	0.4	22 / 2.0
						s	0.5	-63.6	-6.3	1300	390	37 / 2.0
NaT axon	60.0	+55.0	0	0	m^3h	m	0.5	-48.4	7.3	0.5	0.05	22 / 4.0
						h	0.2	-69.0	-5.3	45	0.4	22 / 2.0
NaP soma and prox	0.2	+55.0	-1.0	0.1	mh	m	1.0	-51.3	4.0	18	0.3	22 / 1.0
						h	0.2	-48.4	-10	6s	2s	22 / 1.0
Ih prox	0.004	-25.0	0.4	1	q	q	0.6	-73.0	-7.0	50	19	33 / 4.5
Ih distal	0.004	-25.0	0.4	1	q	q	0.6	-81.0	-7.0	50	19	33 / 4.5
Kdr axon	10.0	-85.0	0	0	n	n	0.8	13.0	11.0	8.0	1.0	22 / 4.0
Kdr other	3.0	-85.0	0	0	n	n	0.8	13.0	11.0	8.0	1.0	22 / 4.0
K-A prox	1.2	-85.0	-0.3	0.1	a^4b	a	0.5	-27.1	22.9	1.0	1.0	35 / 4.0
K-A distal	1.2	-85.0	-0.3	0.1	a^4b	a	0.5	-32.8	19.1	1.0	1.0	35 / 4.0
K-A all						b	0.5	-56.0	-8.0	na	5.0	35 / 1.3
K-M	0.3	-78.0	-1.0	64	m	m	na	-39.8	5.2	150	0.0	30 / 5.0
K-C	0.3	-91.0	0	0	c	c	na	na	na	22	4.0	22 / 4.0
K-AHP	0.5	-91.0	0	0	q	q	na	na	na	22	1.0	22 / 1.0
Ca-T	2.0	GHK	1.0	1.7	m^2h	m	0.7	-36.2	7.0	20	3.0	22 / 1.7
						h	0.8	-80.0	-6.4	35	10.0	22 / 2.5
Ca-R/N	1.5	GHK	0.4	1.6	m^2h	m	0.5	-20.3	9.4	1.2	0.4	22 / 2.0
						h	0.5	-54.0	-9.2	100	100	22 / 2.0
Ca-L	1.2	GHK	0.7	1.7	m^2	m	0.5	-12.2	7.0	1.2	0.4	22 / 2.0

Abbreviations: theoretical maximum conductance (g_{max}), reversal potential (V_{rev}), acetylcholine (ACh), maximum ACh effect (A), half-effect concentration (Kd), variable (var), rated temperature (temp), proximal (prox), not applicable (na), seconds (s), Goldman-Hodgkin-Katz formula (GHK), initial segment (IS), transient sodium channel (NaT), persistent sodium channel (NaP), delayed rectifier (Kdr), type-A potassium channel (K-A), muscarinic potassium current (K-M), calcium-activated potassium channel (K-C), after-hyperpolarization potassium current (K-AHP), type-T low-voltage activated calcium channel (Ca-T), types-R and N medium-voltage activated calcium channels (Ca-R/N), type-L high-voltage activated calcium channel (Ca-L). See equation (5) and associated text for other symbols and terms.

types in the model were chosen based on the ratio of Kdr and K-A found in CA3 pyramidal cells of adult rats (Klee, Ficker, and Heinemann, 1995). K-A channel inactivation is approximately a linear function of the membrane potential and cannot be fit adequately using equation (5). The time constant for K-A inactivation gating is found with the relationship

$$V_{min} = V_0 + \frac{\tau_0}{\eta}$$

$$\tau(V) = \frac{\eta \cdot (V - V_{min}) \cdot Q_{10}^{(T_{rated} - T)/10}}{1 - \exp(-(V - V_{min})/k)} + \tau_0 \qquad (9)$$

where V_0 = -56 mV is the membrane potential at which the empirical linear relationship extrapolates to a zero time constant, η = 0.26 ms/mV is an empirical constant, V_{min} is a value controlling voltages over which the relationship is non-linear, $\tau(V)$ is the time constant of gating variable b, τ_0 is a rate limiting time constant, Q_{10}, T_{rated}, and T are as above, and k = 5 mV is a steepness parameter controlling the approach to a minimum value at hyperpolarized potentials.

Properties of the K-M current are based on measurements using physiological calcium concentrations as opposed to different results obtained with calcium free solutions (Selyanko and Brown, 1999). Time constants for the K-M current are found by

$$\Delta V = V - V_{half},$$

$$\tau(V) = \frac{r \cdot Q_{10}^{(T_{rated} - T)/10}}{\exp\left(\frac{\Delta V}{k_1}\right) + \exp\left(\frac{\Delta V}{k_2}\right)} \qquad (10)$$

where k_1 = 45 mV, k_2 = -10 mV, and the resulting time constant is $\tau(V)$. The value of r is chosen so that for the rated temperature, the maximum resulting time constant has the

τ_{max} value shown in Table S5. The Q_{10} value used in modeling this current is derived from results by Halliwell and Adams (1982).

The calcium-activated potassium channel (K-C) is modeled using the formalism of Moczydlowski and Latorre (1983) with the exception that parameters have been rescaled to conform with calcium concentration sensitivities measured in hippocampal neurons (Gong, Gao, Huang, and Tong, 2001). Activation and deactivation rates without temperature adjustments for K-C are given by

$$\alpha_{bolt} = \frac{0.48\,\text{ms}^{-1} \cdot \chi}{\chi + \frac{k_1}{\kappa_{Ca}} \exp\left(0.84 \cdot \frac{V}{\kappa_V} \cdot \frac{zF}{RT}\right)},$$

$$\beta_{bolt} = \frac{0.28\,\text{ms}^{-1}}{1 + \frac{\chi \cdot \kappa_{Ca}}{k_2} \exp\left(1.0 \cdot \frac{V}{\kappa_V} \cdot \frac{zF}{RT}\right)} \qquad (11)$$

where χ is the calcium concentration, V is membrane potential, k_1=180 μM, k_2=11 μM, κ_{Ca}=16 is a calcium scaling factor, κ_V=1.95 is a voltage scaling factor, and zF/RT is as above.

A simplified model is used to represent the after-hyperpolarization current K-AHP. The current model follows the formalism proposed by Migliore et al. (1995) except that the half-activation value for intracellular calcium has been rescaled to be 600 nM corresponding with experimentally measured values (Hirshchberg, Maylie, Adelman, and Marrion, 1999). Model equations for K-AHP are based on the alpha-beta formalism

$$\alpha = (200\,\text{ms})^{-1} \cdot (\chi/600\,\text{nM})^4,$$
$$\beta = (200\,\text{ms})^{-1} \qquad (12)$$

where α and β are activation and deactivation rates and χ is the microdomain

calcium concentration. In the current model, ACh indirectly modulates K-AHP because calcium influxes for medium and high-voltage activated calcium channels are reduced by ACh modulation. No explicit modulation of K-AHP by ACh is included in the current model. Temperature dependencies are also not addressed in the current model.

Three categories of calcium channels are included in the target cell model. These correspond with low, medium, and high-voltage activated calcium channel types (Fisher, Gray and Johnston, 1990; Takahashi, Ueno, and Akaike, 1991; Brown, Schwindt, and Crill 1993; Magee and Johnston, 1995; Avery and Johnston, 1996; Kavalali et al., 1997). The model for medium-voltage activated calcium currents is a composite of R, N, and possibly P-type calcium channel currents. Low-voltage activation of the L-type calcium channel is not addressed in the current model.

Some channel activation processes do not conform with the assumptions of independent gating. For example, a channel gating expression of m^2h implies that channel activation should be slower than deactivation whereas this may not actually be the case. In such cases, the m^2 term is used in the current model to derive voltage sensitivity, that is the $X_\infty(V)$ term, but gate activation and deactivation rates are determined by the time constant term $\tau(V)$ alone, effectively treating the exponent of m as one in determining channel kinetics. Cases in which this applies are the activation gate of the transient potassium channel K-A (Hoffman et al., 1997; Martina et al., 1998) and activation gating of calcium channels Ca-R and Ca-L (Brown et al., 1993).

Many channels are thought to have uniform properties throughout the cell or else no differences have been experimentally characterized. Channels are represented in the current model as uniformly distributed throughout the soma and dendrites of the target cell. Exceptions to this general rule are NaT, Ih, Kdr, K-A, and K-C channels. These channels have different properties when measured experimentally at proximal locations near the soma and at more distal locations. For the current model, the dendritic region between a point adjacent to the soma and a path distance 150 μm from the soma is assumed to be a region of transition for channel properties. For example, the peak conductivity of K-C channels is reduced over this region and is virtually absent in more distal dendrites (Poolos and Johnston, 1999). This is reflected in the current model as a linear decrease in K-C conductivity from a maximum value adjacent to the soma to zero at dendrite locations with a path distance of 150 μm or more from the soma.

Phosphorylation effects cause a difference in NaT sodium channel properties along the somato-dendritic axis (Gasparini and Magee, 2002). In the current model, this is represented using separate sodium channel models for proximal and distal dendrite channel types. Similarly, regional variations in K-A, and Ih channels have been found experimentally (Hoffman et al., 1997; Magee, 1998). In these cases, channel properties are smoothly blended along the dendrite up to the proximal-distal demarcation point at a path distance of 150 μm from the soma. Activation and inactivation rates for blended channel gates are determined by

$$\rho_{blend} = \min\left(1, x/150\,\mu m\right),$$
$$\alpha_{blend} = \left(1 - \rho_{blend}\right)\alpha_{prox} + \rho_{blend}\,\alpha_{dist}, \qquad (13)$$
$$\beta_{blend} = \left(1 - \rho_{blend}\right)\beta_{prox} + \rho_{blend}\,\beta_{dist}$$

where x is path distance from the soma to the location of the blended channel, ρ_{blend} is the derived blending ratio, α_{prox} and β_{prox} are the activation and deactivation rates for the

proximal form of the channel, α_{dist} and β_{dist} are corresponding rates for the distal form of the channel, and α_{blend} and β_{blend} are resulting blended activation and deactivation rates. Because compartments represent a portion of the dendrite with non-zero extent, channel properties may vary within a compartment. When this is the case, the effective blending ratio is averaged over the extent of the compartment as applicable.

Channel conductivity values are similarly blended smoothly along the extent of the dendrite such that the value used within the compartment represents an average of channel conductivity across the extent of the compartment. In the current model, NaT and K-C conductivities vary over the region up to 150 μm from the soma and then have constant values in more distal locations. Kdr, K-A, and Ih channels increase in conductivity as a linear function of distance from the soma. At 350 μm from the soma, the maximum extent measured experimentally, these channels have increased in conductivity by factors of 0.14, 5.2, and 5.8, respectively, over values found at the soma (g_{max} in Table S5). Experimental finding suggest that K-A channels are more dense in thin oblique dendrites (Frick et al., 2003). To accommodate these findings, K-A channel conductivity in the model is further scaled by a three-halves power law in dendrites whenever the radius is less than 0.4 μm.

Relatively little experimental data exists with regards to channel densities and properties in the basal dendrites of hippocampal pyramidal cells. For the current model, basal dendrites are treated the same as apical dendrites. Path distance from the soma is used in determining channel properties without respect to the apical versus basal distinction in location.

Ion channels of the axon and initial segment are represented in a simplified form in the current model. The initial segment compartment is populated with NaT, Kdr, and K-M channels, each with conductivity and other properties as found in the soma. Axon compartments are populated with the axonal form of transient sodium channels and Kdr potassium channels with conductivity and other properties as shown in Table S5.

Synaptic Connection Models
The density of afferent synaptic connections used in the current model is proportional to the probability of a synaptic connection forming between a dendrite and an axon passing close to it. This method of distributing synapses is consistent with both experimental findings (Liu, 2004) and theoretical analysis (Stepanyants, Hof & Chklovskii, 2002a, 2002b). Synaptic density scales based on the area of a cylinder with a radius 1 μm larger than the associated cylindrical compartment. For each compartment, excitatory synapses are modeled here as occurring at the rate of 0.1 synapses per μm^2 and inhibitory synapses occur at the rate of 0.025 synapses per μm^2. The four-to-one ratio of excitatory-to-inhibitory synapses used here is based on results from hippocampal cell cultures (Liu, 2004).

In the current model, afferent place cells form at most one synaptic connection with the target cell in an appropriate laminar region (Amaral and Witter, 1989; Amaral, Ishizuka, and Claiborne, 1990). Inter-neurons, however, form one or more connections with the target cell, also within the appropriate laminar regions (Miles et al., 1996). The location of synaptic connections is otherwise chosen at random. Initialization the random number algorithm with controlled seed values allows the connection pattern to be reproducible from one simulation run to another.

Synaptic responses are modeled using a dual-exponent formulation (Dayan and

Abbott, 2001). Time delays for neuro-transmitter release are included in the model with a default value of 250 μsec, characteristic of mammalian synapses at physiological temperatures (Sabatini and Regher, 1999).

Table S6 shows synapse model parameters for excitatory glutamatergic synapses in which α-amino-3-hydroxy-5-methyl-4-isoxalone propionic acid (AMPA) and N-methyl-D-aspartate (NMDA) receptors are present. Synapse conductance values shown are for point conductances representing the conductance of a single synapse with g_{max} representing the peak conductance value achieved in response to a single afferent spike that resulted in neurotransmitter release.

NMDA receptor time constants have been found to be dependent on membrane potential (Kampa et al., 2004). The value of τ_{decay} shown in Table S6 is derived from measurements by Flint et al. (1997) and corresponds with an estimate of the decay rate of NMDA receptor currents near cell resting potential. The voltage sensitivity of the NMDA receptor Mg^{2+} pore blocker is a modeled here using the relationship of Jahr and Stevens (1990) as

$$B(V) = \left(1 + \frac{[Mg^{2+}]}{3.57} \exp(0.062 \cdot V)\right)^{-1} \quad (14)$$

where $B(V)$ is the pore blockage ratio, $[Mg^{2+}]$ is the external concentration of Mg^{2+} ions in mM, and V is the membrane potential in mV. In the model, $[Mg^{2+}]$ is assumed to be 1.3 mM, representative of physiological conditions.

NMDA receptor currents have been found to be affected by muscarinic agonists (Grishin, Gee, Gerber, and Benquet, 2004) with synapses in CA3 responding differently from those in CA1. Careful measurement that avoids dialysis of the cell shows that for CA3 pyramidal cells a small increase in NMDA receptor currents in the presence of low concentrations of muscarine. This is incorporated into the current model using the formalism of equation (6) with A=0.39 and Kd = 1 μM ACh. Muscarinic receptor desensitization is not addressed in the current model.

AMPA receptors for CA3-CA3 associational connection (AC) synapses and EC-CA3 perforant path (PP) synapses are affected by synaptic plasticity. The instantaneous value of AMPA receptor conductance varies in proportion to a synaptic weight for these synapse types. The g_{max} value appearing in Table S6 for AC and PP synapses is the conductance when the synaptic weight value is one. Plasticity of DG-CA3 mossy fiber (MF) synapses is not included in the model and the conductance

Table S6. Glutamate synapse model parameters

Receptor Type	g_{max} (nS)	R_{spine} (MΩ)	V_{rev} (mV)	t_{delay} (ms)	τ_{rising} (ms)	τ_{decay} (ms)	Temp / Q_{10}
AMPA (MF)	2.0	0	0	0.25	3.0	3.0	37 / 1.0
AMPA (AC, PP)	1.0	100	0	0.25	0.6	2.5	37 / 1.0
NMDA (NR2A)	0.2	100	0	0.25	2.0	75	25 / 3.0

Abbreviations and symbols: peak conductance (g_{max}), spine neck resistance (R_{spine}), reversal potential (V_{rev}), neurotransmitter release delay (t_{delay}), rising time constant (τ_{rising}), falling time constant (τ_{decay}), rated temperature °C (temp), mossy fiber pathway (MF), CA3 associational connection (AC), perforant pathway (PP). NR2A is an NMDA receptor subunit type.

of these AMPA receptor types does not vary. Synapses with spines are modeled electrically by approximating the spine neck as a series resister (Johnston and Wu, 1995) with a resistance value within the range estimated experimentally (Svoboda, Tank, and Denk, 1996). Including spine necks in the model results in a small adjustment to the peak conductance values of affected synapses. Only the electrical effects of spine necks are addressed in the current model.

Glutamatergic synapses in the hippocampus have variable probabilities of releasing neurotransmitter in response to afferent spikes. For AC and MF synapses, the model of neurotransmitter release is based on the model of Schaffer collateral neurotransmitter release proposed by Dittman, Kreitzer, and Regehr (2000). Model parameters, as shown in Table S7, are adjusted to better conform with experimental findings for CA3 synapses (Salin, Scanziani, Malenka , and Nicoll, 1996). While PP synapses also show variable release patterns, these have not been sufficiently characterized to form a quantitative model. A fixed release probability of 0.25 is used for PP synapses.

Table S7. Glutamate synapse presynaptic plasticity model parameters

Parameter	SC	AC	MF	PP
F_1	0.24	0.24	0.033	0.25
ρ	2.2	2.0	3.14	na
τ_F (ms)	100	100	170	na
τ_D (ms)	50	50	50	na
k_0 (sec^{-1})	2	2	2	na
k_{max} (sec^{-1})	30	30	30	na
K_D	2	2	2	na
NT		1	30	na
Release mode		prob	cont	prob

Abreviations: Schaffer collateral (SC), CA3 associational connection (AC), mossy fiber pathway (MF), perforant path (PP), not applicable (na), probabilistic (prob), continuous (cont). See Dittman, Kreitzer, and Regehr (2000) for parameter definitions and model equations.

Because MF synapses have multiple release sites (Henze, Urban, and Barrionuevo, 2000), MF neurotransmitter release is treated as a continuous value. For other synapses, neurotransmitter release is modeled as a Bernoulli trial probabilistic event.

In CA3, modulation of presynaptic release probabilities by ACh depends on synapse type (Hasselmo, Schnell, Barkai, 1995). AC glutamatergic synapses are affected to a greater extent than PP synapses. Equation (6) approximately fits experimental data for associational synapse effectiveness when A = -0.8 and K_d = 45 µM. This is applied in the current model by adjusting presynaptic release parameter values for affected synapses based on the assumed ACh concentration. Values affected are initial release probability, facilitating, and depressing calcium entry amounts, that is, F1, Δ_F, and Δ_D, respectively.

Table S8 contains parameters used for modeling inhibitory synapses that use the neurotransmitter γ-aminobutyric acid (GABA). Multiple types of GABA synapses are found in CA3 pyramidal cells (Miles et al., 1996; Scanziani, 2000). $GABA_A$ synapses are permeable to Cl$^-$ while $GABA_B$ synapses are coupled via G-protein interactions with K$^+$ permeable channels.

$GABA_A$ synapses at the soma have relatively rapid rise and decay rates when responding to an afferent spike. A slow form of $GABA_A$ synapses has been found in distal dendrites of CA1 pyramidal cells (Banks, Li, and Pearce, 1998). In the current model, slow $GABA_A$ synapses are placed in distal regions of target cell dendrites concomitant with perforant path synapses. $GABA_A$ synapses at the soma are larger than those found in dendrites (Miles et al., 1996). This is represented in the target cell model by decreasing peak $GABA_A$ conductance

Table S8. GABAergic synapse model parameters

Synapse type	g_{max} (nS)	V_{rev} (mV)	ACh A	ACh Kd (μM)	a_0	τ_{ppfd} (ms)	t_{delay} (ms)	τ_{rising} (ms)	τ_{decay} (ms)
GABA$_{A,fast}$	0.2	-70	-0.8	3.3	-0.7	15	0.25	0.3	5.6
GABA$_{A,slow}$	0.2	-70	-0.8	3.3	-0.7	15	0.25	5.0	40
GABA$_B$	0.5 pS	-95	-0.8	3.3	3.7	33	20.0	70	110 (84%) 516 (16%)

Abbreviations and symbols: peak conductance at the soma (g_{max}), reversal potential (V_{rev}), acetylcholine (ACh), maximum ACh effect (A), half-effect concentration (Kd), neurotransmitter release delay (t_{delay}), rising time constant (τ_{rising}), falling time constant (τ_{decay}). Note that g_{max} for GABA$_B$ receptors is a conductance change per afferent GABAergic spike and does not reflect the conductance of associated potassium channels. GABAergic synapse conductance is reduced by a factor of three in dendrites as compared with synapses at the soma.

values in dendrites by a factor of three compared with the corresponding value in the soma.

GABA$_B$ synaptic currents arise through a series of complex interactions. For the purposes of the current model, this is simplified by expressing the result of GABA$_B$ receptor activation with a combination of two dual-exponent responses (Otis, De Koninck, and Mody, 1993). The conductance value used in modeling GABA$_B$ receptors is scaled to correspond with the ratio of charge transfer between GABA$_A$ and GABA$_B$ receptor currents that arise in response to low-frequency afferent spikes (Scanziani, 2000). Slow initial activation of GABA$_B$ receptors is represented in the model as a delay between the arrival of GABAergic spikes and the time at which GABA$_B$ currents are detectable such that the time to peak response in the model closely approximately the time-to-peak for GABA$_B$ responses found by Otis et al. (1993) including the 10 ms overhead interval noted by Otis et al. as preceding the starting time in their plots of measured postsynaptic currents.

Both GABA$_A$ and GABA$_B$ synapses are affected by the frequency of the afferent spike train (Scanziani, 2000). GABAergic synapses are also affected presynaptically by ACh modulation (Seeger et al., 2004). This is reflected in the current model as the product of a paired-pulse effect and a

muscarinic modulation effect as

$$q_{rel} = \left[1 + a_0 \exp\left(-\frac{t_{ISI}}{\tau_{ppfd}}\right)\right] \times \left[1 + \frac{A \cdot [ACh]}{[ACh] + Kd}\right] \quad (15)$$

where q_{rel} is the release quantity, a_0 is the paired-pulse effect for immediately successive afferent spikes, t_{ISI} is the time between spikes, and τ_{ppfd} is the time constant of the paired-pulse effect, [ACh] is the current extracellular ACh concentration, A = -0.8, and Kd = 64 μM. For GABA$_A$ synapses, q_{rel} is interpreted in the model as the probability of neurotransmitter release. For GABA$_B$ synapses, in which the modeled response is more collective, q_{rel} is interpreted as a continuous value for scaling response magnitude. The value of a_0 used in the model of GABA$_B$ synapses is positive to account for facilitation seen in higher frequency stimulations even though, for single spike pairings, GABA$_B$ synapses show paired-pulse depression (Otis et al., 1993; Scanziani, 2000).

Spike-Timing Dependent Plasticity Model
Long-term synaptic plasticity is modeled based on spike-timing dependent plasticity (STDP) as described experimentally in CA3 pyramidal cells (Debanne et al., 1997; Bi
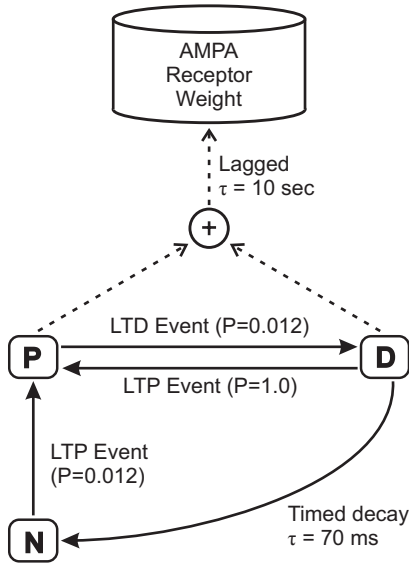
Figure S2. Schematic of model STDP synapse states. Each synapse is assumed to contain a phenomenological population of plasticity entities. Each plasticity entity has a discrete long-term state that influences plasticity expression. The relative AMPA receptor conductance in the synapse, the synaptic weight, exponentially approaches the total fraction of the plasticity population in states P and D with a time constant of 10 sec. Each long-term potentiation (LTP) or long-term depression (LTD) event causes a change of state with probabilities as indicated. Decay from state D to state N occurs with a time constant of 70 msec. Synapses are initially silent, with all plasticity entities in state N. This is figure also appears in the main body of the article and is included here for completeness.

and Poo, 1998). NMDAR-independent long-term plasticity is not addressed within the scope of the current model and thus mossy fiber plasticity is not addressed here.

While it would be desirable to model synaptic plasticity in purely mechanistic terms, accurate biophysical models of the underlying pathways remain elusive. A less detailed phenomenological approach to modeling plasticity is developed here by generalizing the plasticity rules proposed by Sjöstrom, Turrigiano, and Nelson (2001). In the current model, STDP is defined in terms of a Markov model of synaptic states (Figure S2). Separate detectors or pathways

are postulated for events that induce long-term potentiation (LTP) and long-term depression (LTD) as previously proposed (Karmarkar and Buonomano, 2001; Bender, Bender, Brasier, and Feldman, 2006). LTP is assumed to be induced whenever a sufficient number of NMDA receptors containing the NR2A subunit are briefly opened with a combination of glutamate binding and postsynaptic depolarization. Receptor time constants are adapted from experimental results (Flint et al., 1997), adjusted for recently discovered dependencies on the state of the Mg^{2+} pore blocker (Kampa et al., 2004; Vargas-Caballero & Robinson, 2004), and extrapolated to physiological temperatures. The model of STDP incorporated in target cell AMPA receptor synapses uses parameters shown in Table S9.

Table S9. STDP Model Parameters

Parameter	Symbol	Value
Maximum weight	W_{max}	3.2
Weight adjust time constant	τ_W	10 sec
Voltage threshold for LTP	V_{LTP}	-30 mV
Voltage threshold for LTD	V_{LTD}	-40 mV
Minimum postsynaptic ISI	t_{ISI}	3 ms
NMDAR open probability	Po	0.02
Rated temperature for Po	T_{Po}	25°
Q_{10} for Po	Q_{10}	1.8
Num. NMDAR in synapse	N_{NMDAR}	400
Num. NMDAR for LTP	N_{LTP}	5
Glu binding probability	P_{bind}	0.6
Time for NMDAR to open	t_{open}	10 ms
D-state decay time constant	τ_{LTD}	70 ms
Homosynaptic LTD prob.	P_{HLTD}	0.06
LTD probability for $\Delta t=0$	$P0_{LTD}$	0.45
LTD prob. time constant	τ_{PLTD}	90 ms
LTP N-to-P transition prob.	k_{LTP}	0.012
LTD P-to-D transition prob.	k_{LTD}	0.012
LTP D-to-P transition prob.	k_{FDP}	1.0
Ca^{2+} NMDAR supp. amount	A_{CaSupp}	0.3
Ca^{2+} supp. time constant	τ_{CaSupp}	90 ms

Abbreviations: long-term potentiation (LTP), long-term depression (LTD), NMDA receptor (NMDAR), inter-spike interval (ISI), probability of opening (Po), glutamate (Glu), probability (prob), suppression (supp).

The LTP component of the STDP timing curve is established by harmonizing the results that Debanne et al. (1997) measured at 32° with the results obtained by Bi and Poo (1998) at room temperature (nominally 25°). LTD inducing events are determined by the relative timing of pre-and postsynaptic spikes as found by Debanne et al. (1997). As found experimentally, LTP inducing events override immediately preceding LTD events (Sjöstrom et al., 2001; Wang et al., 2005). A form of short-term calcium suppression of NMDA receptors is included in the model because of the extra sensitivity to intracellular calcium found in CA3 NMDA receptor currents (Grishin et al., 2004) and because of the correlation between such sensitivity and the increased temporal window for LTD induction (Froemke, Poo, and Dan 2005) such as found in CA3 pyramidal cells (Debanne et al., 1997). Expression of synaptic plasticity is assumed to occur at a fixed rate, which, while not tightly constrained by experimental data, provides a delay between plasticity inducing events and the full expression of plasticity in the synapse. It should be emphasized that the model of synaptic plasticity used here is entirely phenomenological and aims only to approximate mean values of changes to AMPA receptor currents induced by synaptic plasticity.

Detection of LTP events involves an estimate of the number of concurrently open NMDA receptors at a time when postsynaptic membrane potentials are sufficiently depolarized to remove the Mg^{2+} pore blocker in the NMDA receptor and permit the influx of calcium ions. A simplified model of the synapse is used to make this estimate. A fixed number of NMDA receptors is assumed to be present in the synapse (N_{NMDAR}) of which a fixed proportion of those not current bound are assumed to bind to glutamate (P_{bind})

following each neurotransmitter release event. Glutamate unbinding is assumed to occur at the same rate as NMDA receptor currents in the synaptic model.

LTP events are detected when the postsynaptic membrane potential at the synapse exceeds a voltage threshold (V_{LTP}). The probability of an LTP event in this case is estimated in the current model as

$$A_{AChCa} = 1 - \frac{1 - A_{CaSupp}}{1 + A_{ACh}\dfrac{[ACh]}{[ACh] + Kd}},$$

$$n = N_{glu} \cdot P_o \cdot Q_{10}^{(T - T_{Po})/10}$$

$$\times \left(1 + A_{ACh}\frac{[ACh]}{[ACh] + Kd}\right) \qquad (16)$$

$$\times \left(1 - A_{AChCa}\exp\left(-\frac{\Delta t}{\tau_{CaSupp}}\right)\right),$$

$$P_{LTP} = \frac{n^4}{n^4 + N_{LTP}^{\,4}}$$

where n is the expected number of open NMDA receptors, N_{glu} is the expected number of bound receptors, T is the temperature, A_{ACh} and Kd are the NMDAR ACh modulation parameters described above, Δt is the time since the previous postsynaptic spike event, P_{LTP} is the estimated probability of an LTP event, and other symbols are as shown in Table S9. Parameters for Ca^{2+}-dependent suppression of NMDA receptors are derived by fitting data reported by Froemke, Poo, and Dan (2005). A_{AChCa} combines the effects of ACh modulation and Ca^{2+}-dependent suppression on the assumption that an effect of ACh is to increase the sensitivity of changes to intracellular calcium without changing the maximum effect of Ca^{2+}-dependent suppression when Δt approaches zero. Other parameters are derived from published estimates except for Q_{10} which has been chosen to reconcile STDP results measured

at different temperatures. The Q_{10} value used in equation (16) therefore does not necessarily correspond with the temperature dependence found in NMDA receptor currents.

The probability of LTD inducing events is purely phenomenological without any assumption as to the mechanisms involved. For a given presynaptic spike, let Δt be the time between the spike arrival and the most recent time at which postsynaptic membrane potentials exceeded the LTD threshold (V_{LTD}). The probability of an LTD inducing event for the presynaptic spike is then estimated as

$$P_{LTD} = P_{HLTD}$$
$$+ \left(P0_{LTD} - P_{HLTD}\right) \cdot \exp\left(-\frac{\Delta t}{\tau_{PLTD}}\right) \quad (17)$$

where P_{LTD} is the LTD inducing event probability and parameters are as described in Table S9.

A surprising result reported by Debanne et al. (1997) is that simultaneous pairing of presynaptic and postsynaptic spikes in CA3 pyramidal cells leads to LTD rather than LTP. Debanne et al. offered as an explanation their observation that NMDA receptor currents develop slowly and do not peak until well after the presynaptic spike. For purposes of the current model, during the time interval immediately following a presynaptic spike, both LTP and LTD events are assumed to be possible (Bender et al., 2006). The number of open NMDA receptors is assume to increase linearly over time during the interval in which LTP and LTD overlap, resulting in increasing probabilities of LTP induction. The probability of an LTD inducing event in the overlap interval is estimated as

$$P_{LTD} = \left(P0_{LTD} - P_{HLTD}\right) \cdot \left(1 - \frac{\Delta t}{t_{open}}\right) \quad (18)$$

where P_{LTD} is the probability of an LTD inducing event, $\Delta t < t_{open}$ is the time between the previous presynaptic spike and the time at which the postsynaptic membrane potential threshold was subsequently exceeded, and t_{open} is as described in Table S9. If Δt is not less than t_{open} then P_{LTD} is zero. Note that the preceding presynpatic spike is subject to homosynaptic LTD, which is treated as a separate LTD-inducing event in the model.

Evolution of the Markov state model is as shown in Figure S2. For a given synapse, let N, P, and D be the fraction of the plasticity entity population in the respective states and let W be the current synaptic weight for AMPA receptors in the synapse. The model of synaptic plasticity then evolves according to

$$\frac{dN}{dt} = -k_{LTP}N \cdot P_{LTP}\delta_{LTP}(t) + D/\tau_{LTD},$$
$$\frac{dP}{dt} = \left(k_{LTP}N + k_{FDP}D\right) \cdot P_{LTP}\delta_{LTP}(t)$$
$$- k_{LTD}P \cdot P_{LTD}\delta_{LTD}(t),$$
$$\frac{dD}{dt} = k_{LTD}P \cdot P_{LTD}\delta_{LTD}(t) - D/\tau_{LTD}$$
$$- k_{FDP}D \cdot P_{LTP}\delta_{LTP}(t),$$
$$\frac{dW}{dt} = \left[W_{max} \cdot (P + D) - W\right]/\tau_{W}$$

$$(19)$$

where $\delta_{LTP}(t)$ and $\delta_{LTD}(t)$ have a unit impulse/sec value when LTP or LTD events potentially occur at time t and are zero otherwise. The probabilities of LTP and LTD event occurrence in any instance are P_{LTP} and P_{LTD} as described above. To reduce the burden of continuously updating the state of every synapse, a computational simplification is used in which synaptic weights for each synapse are only updated once per model time step, that is, once per simulated millisecond. Note that the current model only attempts to estimate the expected synaptic weight and does not take

into account the variability that would result if underlying pathways have stochastic properties.

Huang et al. (2005) have recently shown that GABA$_B$ receptor currents are also affected by the same pathway as AMPA-NMDA receptor LTP. While this phenomenon is not as completely characterized as STDP, it plays a potentially significant role in network stability. The following simplified representation of the phenomenon is adopted in the current model.

Plasticity induced changes in AMPA receptor conductance in a synapse are assumed to be mapped to the GABA$_B$ associated conductance in a time delayed fashion. Let W_{AMPA} be the synaptic weight for AMPA receptors in a synapse. The plasticity modulated GABA$_B$ conductance associated with an AMPA-NMDA receptor synapse is governed by

$$\frac{dg}{dt} = \frac{(1 + \rho W_{AMPA})g_0 - g}{\tau} \qquad (20)$$

where g is the portion of GABA$_B$ conductance associated with the AMPA-NMDA receptor, g_0 is the proportional GABA$_B$ conductance when AMPA receptor weights are zero, ρ is a constant reflecting the relative coupling between AMPA and GABA$_B$ receptor weight changes, and τ is the time constant with which GABA$_B$ conductance changes are expressed. For the current model, parameters used are $\rho=4$ and $\tau=60$ sec, though neither value is tightly constrained by available experimental data. The value of g_0 is derived based on the total conductance for GABA$_B$ synapses for a compartment divided by the number of AMPA-NMDA receptor synapses associated with the same compartment.

Target Cell Model Results
While CA3 pyramidal cells have been less extensively studied than CA1 pyramidal cells, key experimental results were used to constrain the target cell compartmental model. Passive cell properties in the model were evaluated using current injection protocols consistent with the experimental methods of Spruston and Johnston (1992). Results are shown in Figure S3. The current-voltage relationship for a minimal current injection (-10 pA) at the soma corresponded with a whole cell input resistance of 93.5 MΩ when [ACh] = 0 μM and 87.5 MΩ when [ACh] = 100 μM (data not shown). Resting potentials at the soma were -69.2 mV and -65.4 mV for [ACh] = 0 and 100 μM, respectively. Because time constants for the Ih current are voltage sensitive, a single passive time constant could be misleading. Fitting voltages changes occurring shortly after the onset of current injection (+0, +5 and +10 ms) to an exponential decay yielded passive time constants of 40 ms and 35 ms for [ACh] = 0 and 100 μM, respectively. A brain temperature of 37° is assumed for the current simulations. As a consequence, resistances would be expected to be somewhat lower and time constants to be faster than corresponding values found by Spruston and Johnston for CA3 pyramidal cells at 32° (Thompson, Masukawa, and Prince, 1985).

A hallmark of CA3 pyramidal cell behavior is the generation of a characteristic bursting pattern (Wong & Prince, 1981). While the objective of the current model is the simulation of cell activity during a theta rhythm state in which ACh concentrations are elevated, reproducing a CA3 pyramidal cell burst with no ACh present is a sensitive test of the ion channel properties assumed in the model. Figure S4A shows a typical burst generated when a brief current injection is applied at the target cell soma compared with the single spike that is generated in response to the same stimulation when ACh
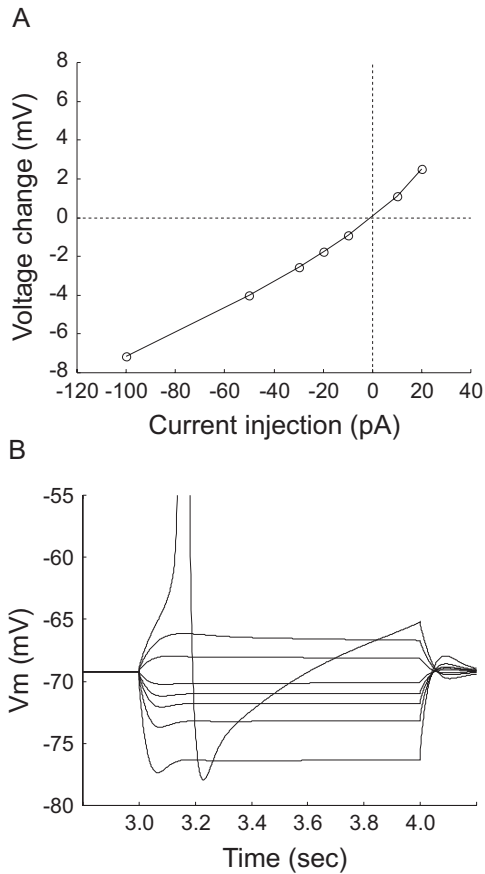
A

B

Figure S3. Measurement of simulated target cell passive properties by somatic current injection. **A.** Whole cell I-V relationship using injections of -100, -50, -30, -20, -10, 10, and 20 pA with [ACh]=0. **B.** Somatic voltage traces. The trace associated with 30 pA current injection is truncated because of spikes generated. The simulated temperature is 37 °C.

is assumed to be present. In the absence of inhibition, action potentials originating in the target cell axon and soma readily backpropagate throughout all dendrites, though with some diminution of amplitude in the more distal locations, as shown in Figure S4B. Throughout the cell, the amplitude of backpropagating action potentials was sufficient to trigger synaptic plasticity changes if paired with presynaptic activity.

The target cell model was modeled with active dendrites. Hence, propagation of synaptic currents from dendrite locations to the soma was potentially non-linear, a factor

that could have affected integration of synaptic inputs.

Figure S5 compares excitatory post-synaptic potentials (EPSP) at the soma resulting from glutamatergic synapse stimulation at two different locations. The first synapse was located on a medium-sized (0.4 μm radius) apical dendrite located 250 μm from the soma and the second was a similar synapse on a thinner (0.24 μm radius) distal dendrite located 550 μm from the soma. While the distal synapse response
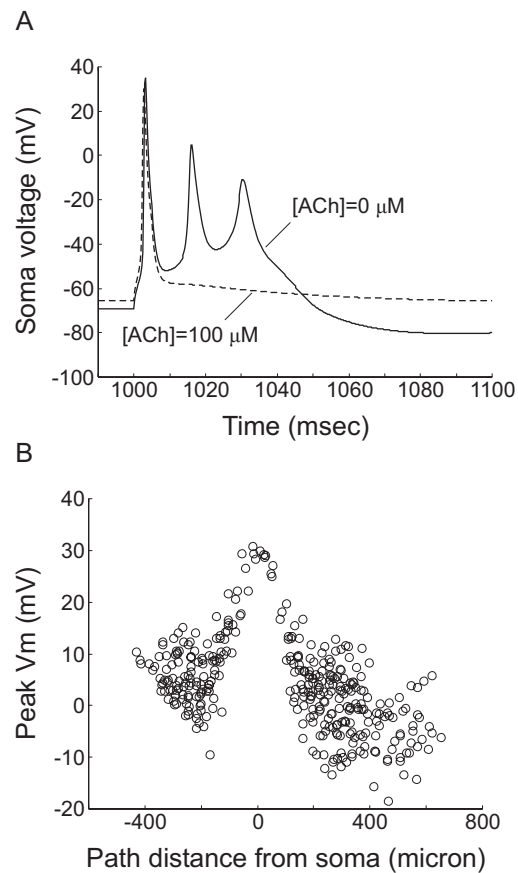
A

B

Figure S4. Simulated target cell responses to a 5 ms somatic current injection of 1 nA following a one second settling interval. **A.** Somatic response showing a characteristic burst response when [ACh]=0 μM and a single spike when [ACh]=100 μM. **B.** Peak dendrite membrane potentials resulting from backpropagating action potentials for [ACh]=100 μM. Peak potentials for [ACh]=0 μM are similar to values shown. Negative path distances refer to basal dendrites.
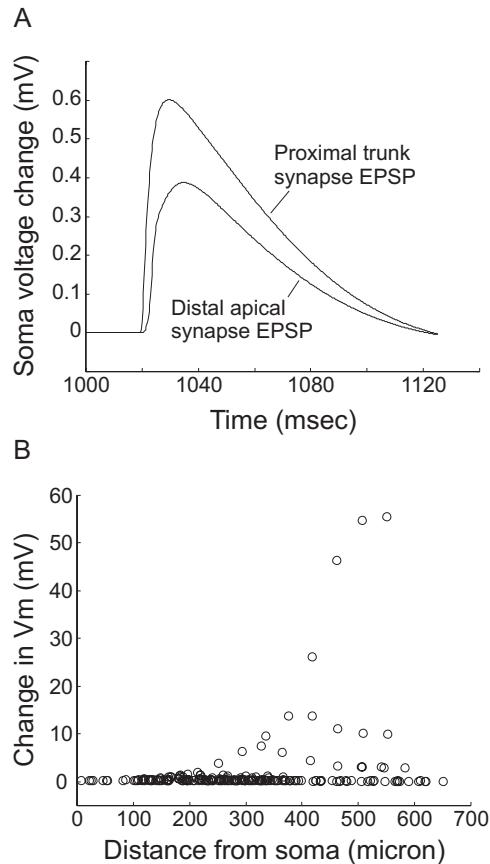
A

B

Figure S5. Simulated responses to glutamatergic synapse stimulation in the target cell. Synapses contain AMPA and NR2A receptors with peak conductance values of 1 nS and 0.2 nS, respectively. **A.** Somatic EPSP response to stimulation of an associational connection synapse located on a medium-sized apical dendrite trunk and to stimulation of a perforant path synapse on a thin distal dendrite. **B.** Peak voltage response to perforant path synapse stimulation. Only responses in apical locations are shown.

showed attenuation at the soma, EPSPs of the two synapses are similar. Peak voltage changes in the dendrites were, however, very dissimilar. The more proximal synapse experienced a peak dendrite depolarization of approximately 5 mV (data not shown) while the distal synapse dendrite depolarization was 56 mV and assumed the form of a local dendritic spike. Even though no action potentials were generated in either case, depolarization of the distal dendrite would have been sufficient to affect NMDA

receptors and induce changes via synaptic plasticity. When sodium channels were suppressed in the target cell model, peak somatic EPSP from distal dendrite synaptic stimulation was reduced by 36% (data not shown) and peak dendritic depolarization was reduced to 27 mV with no evidence of a dendritic spike.

Synaptic Plasticity Results

Two forms of synaptic plasticity are included in the current model. Short-term plasticity affects the probability of neurotransmitter release or, in the case of mossy fiber synapses, the expected quantity of release. Long-term plasticity affects the weight multiplier of AMPA receptor conductance in the synapse.

Figures S6A and S6B compare short-term plasticity in AC and MF glutamatergic synapses. Because ACh affects release in AC synapses, a medium concentration of ACh is assumed in illustrating the effects of short-term plasticity in these synapses. Short-term plasticity in AC synapses was modeled as similar to the model proposed by Dittman et al. (2000) for CA1 Schaffer collateral synapses. The MF short-term plasticity model was constrained by measurements of paired-pulse facilitation for successive spikes and maximum facilitation in a train of spikes (Salin et al., 1996). Frequency dependencies of MF synapse responses have not been completely characterized experimentally, but the current model is consistent with the observation that multiple DG granule cell spikes in rapid succession are needed to produce the quantity of neurotransmitter release required to generate an action potential in a CA3 pyramidal cell (Henze, Wittner, and Buzsáki, 2002).

Figure S6C shows the effect of spike timing in the STDP model of CA3 long-term plasticity for single spike pairings. This is experimentally comparable with
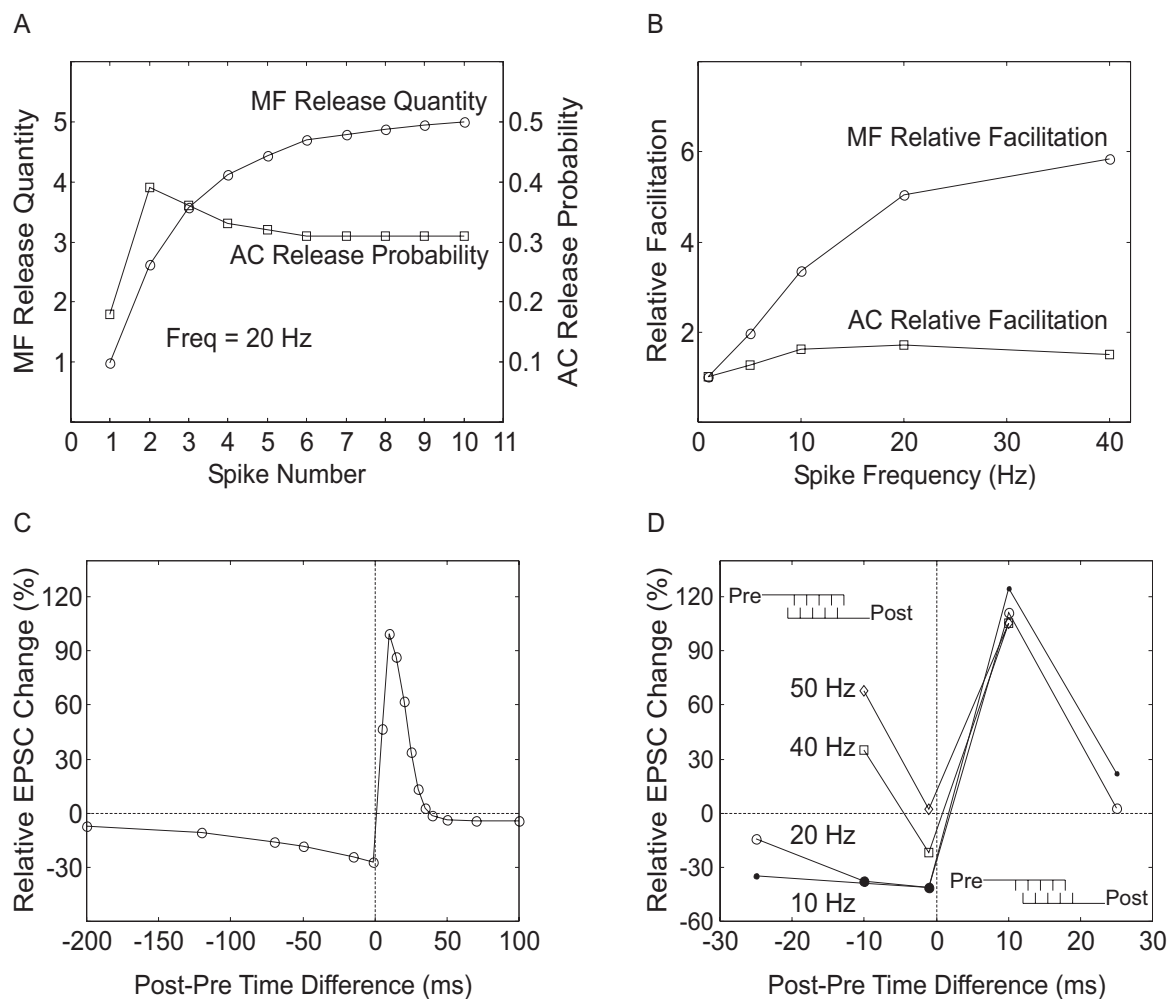
Figure S6. Simulated glutamatergic synaptic plasticity. Results shown are for a simulated temperature of 37° and [ACh] = 20 μM. **A**. Mean neurotransmitter release quantity for each spike in a 20 Hz spike train for mossy fiber (MF) synapses and CA3 associational connection (AC) synapses. Note different scales for each synapse type. AC neurotransmitter release occurs as a single quantile with probabilities as indicated. **B**. Mean release quantity relative to the release rate of the first spike at different frequencies. Value shown is mean release quantity for the tenth spike. **C**. Spike-timing dependent plasticity (STDP) long-term EPSC changes for AC synaptic AMPA receptors. Synaptic weights are set to unity at the start of the simulation and neurotransmitter release probability is set to one throughout. Relative EPSC values are measured via synaptic weights following 60 pre- and postsynaptic spike pairings at one second intervals with an additional 30 second delay after the last spike pairing. Positive time differences correspond with pre- before post spike pairings. **D**. The effect of spike train frequency on synaptic plasticity. Sets of five pre- and postsynaptic spike trains at the frequencies indicated are paired twenty times at three-second intervals. Spike time differences reflect the relative timing of the initial pre- and postsynaptic spikes in each set of five spikes.

experimental results of Debanne et al. (1995) in CA3 pyramidal cells and is similar to results of by Sjöström et al. (2001) for visual cortex L5 pyramidal cells. The initial synaptic weight for these tests was assumed to be one. In general, smaller initial synaptic weights would result in larger relative changes in synaptic weights for LTP spike pairings and should not affect relative changes for LTD pairings.

As found by Sjöström et al. (2001), STDP is dependent upon spike rate as well as timing. Figure S6D shows the affect of multiple pairings of spike trains that have different frequencies. At higher frequencies, LTP dominates over LTD even when postsynaptic spikes precede presynaptic spikes. While, these frequencies are generally in excess of the CA3 pyramidal cell place cell firing rates, they can easily be attained during short bursts.

The effects of ACh on STDP have not been characterized experimentally. The simulations shown in Figure S6 were performed assuming [ACh] = 20 μM, a value sufficiently large to exceed the threshold for muscarinic receptor activation but less than the peak values found during locomotion.

References

Amaral DG, Ishizuka N, Claiborne B (1990) Neurons, numbers and the hippocampal network. Progress in Brain Research 83: 1-11.

Amaral DG, Witter MP (1989) The three-dimensional organization of the hippocampal formation: a review of anatomical data. Neuroscience 31: 571-591.

Avery RB, Johnston D (1996) Multiple channel types contribute to the low-voltage-activated calcium current in hippocampal CA3 pyramidal neurons. Journal of Neuroscience 16: 5567-5582.

Banks MI Li T-B, Pearce RA (1998) The synaptic basis of GABA$_{A,slow}$. Journal of Neuroscience 18: 1305-1317.

Bender VA, Bender KJ, Brasier DJ, Feldman DE (2006) Two coincidence detectors for spike timing-dependent plasticity in somatosensory cortex. Journal of Neuroscience 26: 4166-4177.

Bi G-q, Poo M-m (1998) Synaptic modifications in cultured hippocampal neurons: dependence on spike timing, synaptic strength, and postsynaptic cell type. Journal of Neuroscience 18: 10464-10472.

Borg-Graham L (1999) Interpretation of data and mechanisms for hippocampal cell models. In: Ulinsky PS ed. Cerebral cortex, vol. 13: models of cortical circuits. Springer, New York. http://www.neurophys.biomedicale.univ-paris5.fr/~graham/surf-hippo-files/borg-graham.hpc-models.ps.gz. Cited 27 April 2004.

Brazhnik ES, Muller RU, Fox SE (2003) Muscarinic blockade slows and degrades the location-specific firing of hippocampal pyramidal cells. Journal of Neuroscience 23: 611-621.

Brown AM, Schwindt PC, Crill WE (1993) Voltage dependence and activation kinetics of pharmacologically defined components of the high-threshold calcium currents in rat neocortical neurons. Journal of Neurophysiology 70(4): 1530-1543.

Buzsáki G (2002) Theta oscillations in the hippocampus. Neuron 33: 325-340.

Colbert CM, Pan E (2002) Ion channel properties underlying axonal action potential initiation in pyramidal neurons. Nature Neuroscience 5: 533-538.

Csicsvari J, Jamieson B, Wise KD, Buzsáki G (2003) Mechanisms of gamma oscillations in the hippocampus of the behaving rat. Neuron 37: 311-322.

Dayan P, Abbott LF (2001) Theoretical neuroscience: computational and mathematical modeling of neural systems. MIT Press, Cambridge MA.

Debanne D, Gähwiler BH, Thompson SM (1998) Long-term synaptic plasticity between pairs of individual CA3 pyramidal cells in rat hippocampal slice cultures. Journal of Physiology 507: 237-247.

Dittman JS, Kreitzer AC, and Regehr WG (2000). Interplay between facilitation, depression, and residual calcium at three presynaptic terminals. Journal of. Neuroscience. 20, 1374-1385.

Fisher RE, Gray R, Johnston D (1990) Properties and distribution of single voltage-gated calcium channels in adult hippocampal neurons. Journal of Neurophysiology 64: 91-104.

Flint AC, Maisch US, Weishaupt JH, Kriegstein AR, Monyer H (1997) NR2A subunit expression shortens NMDA receptor synaptic current in developing neocortex. Journal of Neuroscience 17: 2469-2476.

Fox SE, Wolfson S, Ranck JB Jr. (1986) Hippocampal theta rhythm and firing of neurons in walking and urethane anesthetized rats. Experimental Brain Research 62: 495-508.

Frick A, Magee J, Koester HJ, Migliore M, Johnston D (2003) Normalization of Ca^{2+} signals by small oblique dendrites of CA1 pyramidal neurons. Journal of Neuroscience 23(8): 3243-3250.

Froemke RC, Poo M-m, Dan Y (2005). Spike-timing-dependent synaptic plasticity depends on dendritic location. Nature 434: 221-225.

Fyhn M, Molden S, Witter MP, Moser EI, Moser MB (2004) Spatial representation in the entorhinal cortex. Science 305: 1258-1264.

Gasparini S, Magee JC (2002) Phosphorylation-dependent differences in the activation properties of distal and proximal dendritic Na^+ channels in rat CA1 hippocampal neurons. Journal of Physiology 541.3, 665-672.

Gong L-W, Gao T-M, Huang H, Tong Z (2001) Properties of large conductance calcium-activated potassium channels in pyramidal neurons from the hippocampal CA1 region of adult rats. Japanese Journal of Physiology 51: 725-731.

Grishin AA, Gee CE, Gerber U, Benquet P (2004). Differential calcium-dependent modulation of NMDA currents in CA1 and CA3 hipppocampal pyramidal cells. Journal of Neuroscience 24(2): 350-355.

Guérineau NC, Bossu J-L, Gähwiler BH, Gerber U (1995) Activation of a nonselective cationic conductance by metabotropic glutamatergic and muscarinic agonists in CA3 pyramidal neurons of the rat hippocampus. Journal of Neuroscience 15: 4395-4407.

Halliwell JV, Adams PR (1982) Voltage-clamp analysis of muscarinic excitation in hippocampal neurons. Brain Research 250: 71-92.

Hartley T, Burgess N, Lever C, Cacucci F, O'Keefe J (2000) Modeling place fields in terms of the cortical inputs to the hippocampus. Hippocampus 10: 369-379.

Hasselmo ME, Schnell E, Barkai E (1995) Dynamics of learning and recall at excitatory recurrent synapses and cholinergic modulation in rat hippocampal region CA3. Journal of Neuroscience 15: 5249-5262.

Henze DA, Urban NN, Barrionuevo G (2000) The multifarious hippocampal mossy fiber pathway: a review. Neuroscience 98: 407-427.

Henze DA, Wittner L, Buzsáki G (2002) Single granule cell reliably discharge targets in the CA3 hippocampal network *in vivo*. Nature Neuroscience 5(8): 790-795.

Hines ML, Morse T, Migliore M, Carnevale NT, Shepherd GM (2004) ModelDB: A database to support computational neuroscience. Journal of Computational Neuroscience 17: 7-11. Online materials at http://senselab.med.yale.edu/senselab/ModelDB/. Accessed 21 August 2006.

Hirschberg B, Maylie J, Adelman JP, Marrion NV (1999) Gating properties of single SK channels in hippocampal CA1 pyramidal neurons. Biophysical Journal 77: 1905-1913.

Hodgkin AL, Huxley AF (1952) A quantitative description of membrane current and its application to conduction and excitation in nerve. Journal of Physiology 117: 500-544.

Hoffman DA, Magee JC, Colbert CM, Johnston D (1997) K^+ channel regulation of signal propagation in dendrites of hippocampal cells. Nature 387(6636): 869-875.

Huang CS, Shi S-H, Ule J, Ruggiu M, Barker LA, Darnell RB, Jan YN, Jan YL (2005) Common molecular pathways mediate long-term potentiation of synaptic excitation and slow synaptic inhibition. Cell 123, 105-118.

Jaffe DB, Ross WN, Lisman JE, Lasser-Ross N, Miyakawa H, Johnston D (1994) A model for dendritic Ca^{2+} accumulation in hippocampal pyramidal neurons based on fluorescence imaging measurements. Journal of Neurophysiology 71: 1065-1077.

Jahr CE, Stevens CF (1990) Voltage dependence of NMDA-activated macroscopic conductances

predicted by single-channel kinetics. Journal of Neuroscience 10: 3178-3182.

Johnston D, Wu SM-S (1995) Foundations of cellular neurophysiology. MIT Press, Cambridge MA.

Jung MW , McNaughton BL (1993) Spatial selectivity of unit activity in the hippocampal granular layer. Hippocampus 3: 165-182.

Káli S, Dayan P (2000) The involvement of recurrent connections in area CA3 in establishing the properties of place fields: a model. Journal of Neuroscience 20: 7463-7477.

Kampa BM, Clements J, Jonas, P, Stuart GJ (2004) Kinetics of Mg^{2+} unblock of NMDA receptors: implications for spike-timing dependent synaptic plasticity. Journal of Physiology 556: 337-345.

Karmarkar UR, Buonomano DV (2001) A model of spike-timing dependent plasticity: one or two coincidence detectors. Journal of Neurophysiology 88: 507-513.

Kavalali ET, Zhuo M, Bito H, Tsien RW (1997) Dendritic Ca^{2+} channels characterized by recordings from isolated hippocampal dendritic segments. Neuron 18: 651-663.

Klausberger T, Magill PJ, Márton LF, Roberts JDB, Cobden PM, Buzsáki G, Somogyi P (2003) Brain-state- and cell-type-specific firing of hippocampal interneurons *in vivo*. Nature 421: 844-848.

Klausberger T, Márton LF, Baude A, Roberts JDB, Magill PJ, Somogyi P (2004) Spike timing of dendrite-targeting bistratified cells during hippocampal network oscillations *in vivo*. Nature Neuroscience 7: 41-47.

Klee R, Ficker E, Heinemann U (1995) Comparison of voltage-dependent potassium currents in rat pyramidal neurons acutely isolated from hippocampal regions CA1 and CA3. Journal of Neurophysiology 74(5): 1982-1995.

Liu G (2004) Local structural balance and functional interaction of excitatory and inhibitory synapses in hippocampal dendrites. Nature Neuroscience 7: 373-379.

Magee JC (1998) Dendritic hyperpolarization-activated currents modify the integrative properties of hippocampal CA1 pyramidal neurons. Journal of Neuroscience 18: 7613-7624.

Magee JC, Johnston D (1995). Characterization of single voltage-gated Na^+ and Ca^{2+} channels in apical dendrites of rat CA1 pyramidal neurons. Journal of Physiology 487: 67-90.

Magistretti J, Alonso A (1999) Biophysical properties and slow voltage-dependent inactivation of a sustained sodium current in entorhinal cortex layer-II principal neurons: a whole cell and single-channel study. Journal of General Physiology 114: 491-509.

Magistretti J, Alonso A (2002) Fine gating properties of channels responsible for persistent sodium current generation in entorhinal cortex neurons. Journal of General Physiology 120: 855-873.

Marrion NV, Tavalin SJ (1998) Selective activation of Ca^{2+}-activated K^+ channels by co-localized Ca^{2+} channels in hippocampal neurons. Nature 395: 900-905.

Martina M, Schultz JH, Ehmke H, Monyer H, Jonas P 1998. Functional and molecular differences between voltage-gated K^+ channels of fast-spiking interneurons and pyramidal neurons of rat hippocampus. Journal of Neuroscience 18(20), 8111-8125.

Menschik ED, Finkel LH (2000) Cholinergic neuromodulation of an anatomically reconstructed hippocampal CA3 pyramidal cell. Neurocomputing 32-33: 197-205.

Mickus T, Jung H-y, Spruston N (1999) Properties of slow, cumulative sodium channel inactivation in rat hippocampal CA1 pyramidal neurons. Biophysical Journal 76: 846-860.

Migliore M, Cook EP, Jaffe DB, Turner DA, Johnston D (1995) Computer simulations of morphologically reconstructed CA3 hippocampal neurons. Journal of Neurophysiology 73:1157-1168.

Miles R, Tóth K, Gulyás AI, Hájos N, Freund TF (1996) Differences between somatic and dendritic inhibition in the hippocampus. Neuron 16: 815-823.

Moczydlowski E, Latorre R (1983). Gating kinetics of Ca^{2+}-activated K^+ channels from rat muscle incorporated into planar lipid bilayers. Journal of General Physiology 82: 511-542.

Muller RU, Kubie JL, Ranck JB Jr. (1987) Spatial firing patterns of hippocampal complex-spike cells in a fixed environment. Journal of Neuroscience 7: 1935-1950.

Nakazawa K, Quick MC, Chitwood RA, Watanabe M, Yeckel MF, Sun LD, Kata A, Carr CA, Johnston D, Wilson MA, Tonegawa S (2002) Requirement for hippocampal CA3 NMDA receptors in associative memory recall. Science 297: 211-218.

O'Keefe J, Burgess N (1996) Geometric determinants of the place fields hippocampal neurons. Nature 381: 425-428.

O'Keefe J, Burgess N (2005) Dual phase and rate coding in hippocampal place cells: theoretical significance and relationship to entorhinal grid cells. Hippocampus 15: 853-866.

O'Keefe J, Recce ML (1993) Phase relationship between hippocampal place units and the EEG theta rhythm. Hippocampus 3(3): 317-330.

Otis TS, De Koninck Y, Mody I (1993) Characterization of synaptically elicited $GABA_B$ responses using patch-clamp recordings in rat hippocampal slices. Journal of Physiology 463: 391-407.

Pan E and Colbert CM (2001) Subthreshold inactivation of Na^+ and K^+ channels supports activity-dependent enhancement of back-propagating action potentials in hippocampal CA1. Journal of Neurophysiology 85: 1013-1016.

Poolos NP, Johnston D (1999) Calcium-activated potassium conductances contribute to action potential repolarization at the soma but not the dendrites of hippocampal CA1 pyramidal neurons. Journal of Neuroscience 19: 5205-5212.

Quirk GJ, Muller RU, Kubie JL, Ranck JB Jr. (1992) The positional firing properties of medial entorhinal neurons: description and comparison with hippocampal place cells. Journal of Neuroscience 12: 1945-1963.

Sabatini BL, Oertner TG, Svoboda K (2002) The life cycle of Ca^{2+} ions in dendritic spines. Neuron 33: 439-452.

Sabatini BL, Regher WG (1999) Timing of synaptic transmission. Annual Review of Physiology 61: 521-542.

Salin PA, Scanziani M, Malenka RC, Nicoll RA (1996) Distinct short-term plasticity at two excitatory synapses in the hippocampus. Proceedings of the National Academy of Sciences, USA 93, 13304-13309.

Scanziani M (2000) GABA spillover activates postsynaptic $GABA_B$ receptors to control rhythmic hippocampal activity. Neuron 25: 673-681.

Seeger T, Fedorova I, Zheng F, Miyakawa T, Koustova E, Gomeza J, Basile AS, Alzheimer C, Wess J (2004). M_2 Muscarinic acetylcholine receptor knock-out mice show deficits in behavioral flexibility, working memory, and hippocampal plasticity. Journal of Neuroscience 24: 10117-10127.

Segev I, Burke RE (1998) Compartmental models of complex neurons. In: C Koch and I Segev, ed. Methods in neuron modeling: from ions to networks, 2nd edition. MIT Press, Cambridge, MA. pp. 93-136.

Selyanko AA, Brown DA (1999) M-channel gating and simulation. Biophysical Journal 77:701-713.

Sjöström PJ, Turrigiano GG, Nelson SB (2001) Rate, timing, and cooperativity jointly determine cortical synaptic plasticity. Neuron 32: 1149-1164.

Skaggs WE, McNaughton BL, Wilson MA, Barnes CA (1996) Theta phase precession in hippocampal neuronal populations and the compression of temporal sequences. Hippocampus 6:149-172.

Spruston N, Johnston D (1992) Perforated patch-clamp analysis of the passive membrane properties of three classes of hippocampal neurons. Journal of Neurophysiology 67: 508-529.

Stepanyants A, Hof PR, Chklovskii DB (2002a) Information storage capacity of synaptic connectivity patterns. Neurocomputing 44-46: 661-665.

Stepanyants A, Hof PR, Chklovskii DB (2002b) Geometry and structural plasticity of synaptic connectivity. Neuron 34: 275-288.

Stewart M, Quirk GJ, Barry M, Fox SE (1992) Firing relations of medial entorhinal neurons to the hippocampal theta rhythm in urethane anesthetized and walking rats. Experimental Brain Research 90: 21-28.

Svoboda K, Tank DW, Denk W (1996) Direct measurement of coupling between dendritic spines and shafts. Science 272, 716-719.

Takahashi K, Ueno S, Akaike N (1991) Kinetic properties of T-type Ca^{2+} currents in isolated rat hippocampal CA1 neurons. Journal of Neurophysiology 65: 148-155.

Thompson SM, Masukawa LM, Prince DA (1985) Temperature dependence of intrinsic membrane properties and synaptic potentials in hippocampal CA1 neurons *in vitro*. Journal of Neuroscience 5: 817-824.

Tsubokawa H, Ross WN (1997) Muscarinic modulation of spike backpropagation in the apical dendrites of hippocampal CA1 pyramidal neurons. Journal of Neuroscience 17: 5782-5791.

Turner DA, Li X-G, Pyapali GK, Ylinen A, Buzsaki G (1995) Morphometric and electrical properties of reconstructed hippocampal CA3 neurons recorded in vivo. Journal of Comparative Neurology 356: 580-594. http://neuron.duke.edu/cells/. Cited 7 April 2004.

Vargas-Caballero M, Robinson HPC (2004) Fast and slow voltage-dependent dynamics of magnesium block in the NMDA receptor: the asymmetric trapping block model. Journal of Neuroscience 24: 6171-6180.

Vazdarjanova A, Guzowski JF (2004) Differences in hippocampal neuronal population responses to modifications of an environmental context: evidence for distinct, yet complementary, functions of CA3 and CA1 ensembles. Journal of Neuroscience 24: 6489-6496.

Wallenstein GV, Hasselmo ME (1997) GABAergic modulation of hippocampal population activity: sequence learning, place field development, and the phase precession effect. Journal of Neurophysiology 78: 393-408.

Wang H-X, Gerkin RC, Nauen DW, Ni G-Q (2005) Coactivation and timing-dependent integration of synaptic potentiation and depression. Nature Neuroscience 8: 187-193.

Wilson MA, McNaughton BL (1993) Dynamics of the hippocampal ensemble code for space. Science 261(5124): 1055-1058.

Wong RKS, Prince DA (1981) Afterpotential generation in hippocampal pyramidal cells. Journal of Neurophysiology 45: 86-97.